NANO LETTERS

pubs.acs.org/NanoLett Letter

Ultrafast Nanoimaging of Electronic Coherence of Monolayer WSe_2

Wenjin Luo, Benjamin G. Whetten, Vasily Kravtsov, Ashutosh Singh, Yibo Yang, Di Huang, Xinbin Cheng, Tao Jiang,* Alexey Belyanin,* and Markus B. Raschke*

Cite This: *Nano Lett.* 2023, 23, 1767−1773 Read Online

ACCESS | Metrics & More | Article Recommendations | Supporting Information

ABSTRACT: Transition-metal dichalcogenides (TMDs) have demonstrated a wide range of novel photonic, optoelectronic, and correlated electron phenomena for more than a decade. However, the coherent dynamics of their excitons, including possibly long dephasing times and their sensitivity to spatial heterogeneities, are still poorly understood. Here we implement adiabatic plasmonic nanofocused four-wave mixing (FWM) to image the coherent electron dynamics in monolayer WSe_2. We observe nanoscale heterogeneities at room temperature with dephasing ranging from $T_2 \lesssim 5$ to $T_2 \gtrsim 60$ fs on length scales of 50−100 nm. We further observe a counterintuitive anticorrelation between FWM intensity and T_2, with the weakest FWM emission at locations of longest coherence. We interpret this behavior as a nonlocal nano-optical interplay between spatial coherence of the nonlinear polarization and disorder-induced scattering. The results highlight the challenges associated with heterogeneities in TMDs limiting their photophysical properties, yet also the potential of their novel nonlinear optical phenomena.

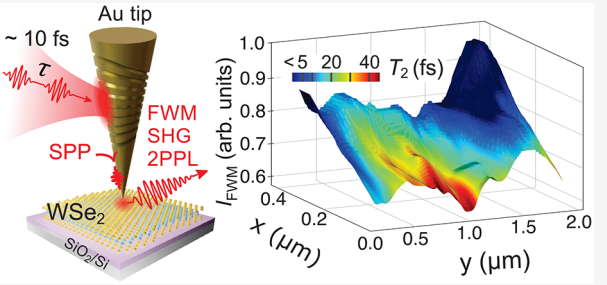

KEYWORDS: *monolayer WSe_2, four-wave mixing nanoimaging, nonlinear optics, electronic coherence and dephasing, decoherence and disorder*

The discovery of the indirect to direct band gap transition in two-dimensional (2D) transition-metal dichalcogenides (TMDs) over one decade ago[1−3] has opened the new field of 2D semiconductor nanophotonics based on a wide range of novel photonic and optoelectronic properties.[4,5] Because of Berry phase physics and strong spin−orbit coupling, TMD monolayers exhibit extraordinary spin and valley phenomena.[6−8] In addition, twisted homo- and heterobilayer structures provide for emerging quantum phenomena and novel correlated electron phases.[9] Owing to the spatial confinement and reduced screening in 2D materials, the exciton light−matter interaction is enhanced, with high oscillator strength and large optical nonlinearity that can be orders of magnitude stronger than in conventional semiconductors.[10−12] These extraordinary optical properties call for an understanding of the underlying exciton coherence.

In previous works, long dephasing times (T_2) have been measured, suggesting TMDs as potential candidates for quantum information applications.[13,14] However, even at low temperature, T_2 for monolayers of MoS_2, $MoSe_2$, and WSe_2 does not generally exceed 200−600 fs as measured with four-wave mixing (FWM) photon echo and multidimensional coherent spectroscopy (MDCS).[10,15,16] Only for monolayer $MoSe_2$ encapsulated by hexagonal boron nitride (h-BN) have exceptionally long T_2 times been measured, with values up to ∼1 ps at 65 K and 3.3 ps at 5 K.[17] These results suggest exciton−exciton and exciton−phonon interactions as primary mechanisms of decoherence,[10,18] with the strong exciton−phonon interaction expected to dramatically shorten T_2 toward room temperature. In addition, inhomogeneous broadening associated with defects, substrate interactions, and other spatial heterogeneities dominate the optical response from the atomic to micrometer scale and further shorten T_2.[19−21]

While the coherent dynamics is thus expected to be controlled on both nanometer length scales and femtosecond time scales, no ultrafast nanoimaging experiments have yet addressed the relationship between exciton coherence and spatial heterogeneity at room temperature. Here, we perform spatiospectral and spatiotemporal tip-enhanced nanoimaging in coherent FWM. In two-pulse correlation nano-FWM imaging, we probe the exciton coherence in monolayer WSe_2 with simultaneous spatial and temporal resolutions of tens of nanometers and a few femtoseconds, respectively. We observe room-temperature dephasing times of the nonlinear polarization ranging from $\lesssim 5$ fs to $\gtrsim 60$ fs, varying over length scales of tens to hundreds of nanometers. Significantly, we observe a counterintuitive spatial anticorrelation between FWM signal intensity and dephasing time, which we interpret

Received: November 18, 2022
Revised: February 19, 2023
Published: February 24, 2023

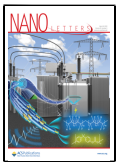

https://doi.org/10.1021/acs.nanolett.2c04536
Nano Lett. 2023, 23, 1767−1773

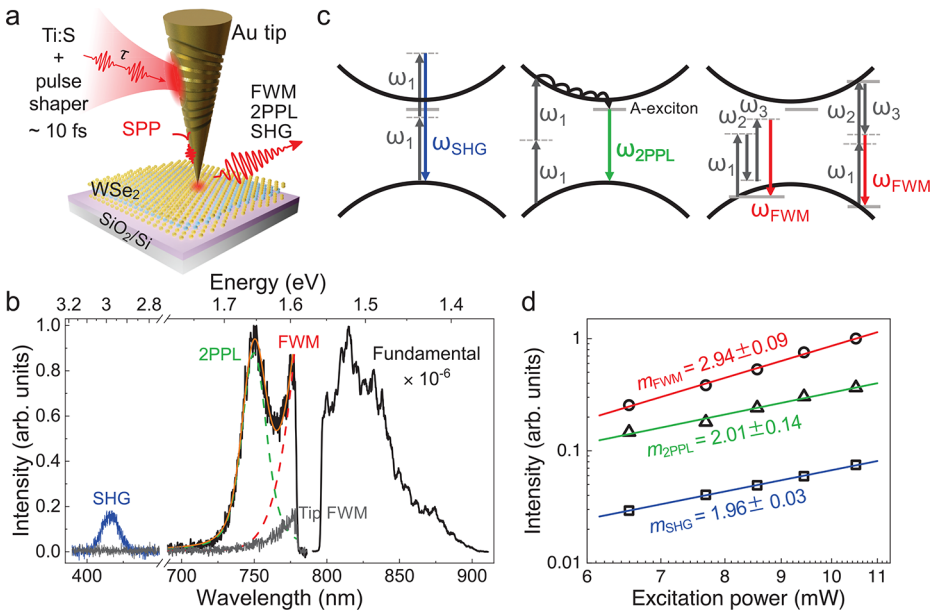

Figure 1. Nonlinear nanospectroscopy of WSe_2. (a) A pair of few-femtosecond pulses of variable time delay are grating coupled and adiabatically nanofocused at the tip apex. The few-nanometer spatial localization gives rise to tip-enhanced nonlinear signal generation in monolayer WSe_2. (b) Nonlinear tip-enhanced spectra from monolayer WSe_2 (black solid line) attributed to and fit as SHG (blue solid line), 2PPL (green dashed line), and FWM (red dashed line), excited by the fundamental pump light (black). For comparison, the nonlinear optical signal from the tip apex itself is shown (gray). (c) Illustration of corresponding nonlinear optical pathways with degenerate FWM dominated by the A-exciton resonance. (d) Power dependence of WSe_2 near-field SHG (blue), 2PPL (green), and FWM (red), with their expected quadratic and cubic dependences, where the power index is labeled by *m*.

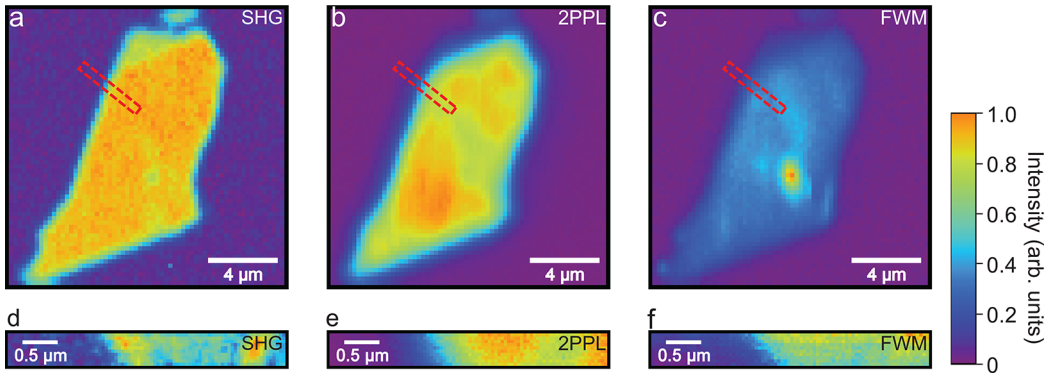

Figure 2. Nonlinear micro- and nanoimaging of monolayer WSe_2. (a–c) Microimages of SHG, 2PPL, and FWM, respectively, showing a low level of spatial heterogeneity. (d–f) Nanoimages of SHG, 2PPL, and FWM, respectively, of a small area (marked by the red dashed rectangles in the microimages) across the monolayer edge showing high spatial variation in SHG due to structural symmetry selectivity.

as an interplay between spatial coherence of the nonlinear polarization and disorder-induced scattering. These results highlight not only the fundamental challenges associated with the wide range of heterogeneities in TMDs but also the potential of new coherence and nonlocal nonlinear phenomena in 2D materials at the nanoscale.

For the measurements, we use adiabatic nanofocused FWM with few-femtosecond pulses and deterministic pulse shaping as developed and described previously[22−24] and shown in Figure 1a. Briefly, plasmonic grating-coupled broad-band femtosecond pulses from a Ti:sapphire oscillator (nominal pulse duration ∼10 fs) are spatially compressed through a conical waveguide transformation.[22,24] The phase and amplitude of the nanoconfined femtosecond pulses at the tip apex are further controlled by a home-built pulse shaper using multiphoton intrapulse interference phase scans (MIIPS) with second-harmonic generation (SHG) from the tip apex serving as feedback, to compensate for the plasmon-propagation-induced dispersion.[22−24] The pulse shaper also generates a pulse replica and controls its relative time delay (τ) for time-resolved two-pulse correlation FWM measurements.

Gold tips were prepared by electrochemical etching, engraved with a grating using focused ion beam milling, and mounted in a shear-force tuning-fork-based atomic force microscope. The WSe_2 monolayers were prepared by exfoliation from bulk WSe_2 crystals (2Dsemiconductors, Scottsdale, AZ, USA) and transferred onto a Si substrate with 300 nm SiO_2 using polydimethylsiloxane (PDMS).[25] (For further experimental details and sample characterization see Figure S1.)

The short wavelength tail of the pump light is filtered out to enable detection of the FWM signal generated in that spectral range. Figure 1b shows the tip-scattered pump and emission spectra with the tip in shear-force feedback on the WSe_2

https://doi.org/10.1021/acs.nanolett.2c04536
Nano Lett. 2023, 23, 1767−1773

monolayer. The excitation spectrum spans from ∼785 to 900 nm and drives three nonlinear optical processes. As shown in Figure 1c, SHG results from the broken centrosymmetry of the WSe_2 monolayer. Incoherent two-photon photoluminescence (2PPL) occurs at the A-exciton resonance after electron−hole pair relaxation. Finally, coherent intrapulse nanolocalized FWM arises from the broad-band pump interacting with the A-exciton resonance. The corresponding power dependences of the three signals are shown in Figure 1d, scaling as expected in second order for SHG and 2PPL and third order for FWM. The onset of tip and sample damage limits the excitation to a maximum of ∼12 mW average power.

For comparison, the signal from the tip itself, when not in near-field contact, only exhibits weak FWM (gray line in Figure 1b). We deconvolute the spectrally overlapping 2PPL (green dashed line) and FWM (red dashed line) spectra by fitting the total spectrum (black line) to a double-Voigt profile. Of the two possible FWM pathways, we expect our signal to be dominated by the triply degenerate case, close to the single-photon resonance with the A-exciton (Figure 1c, left pathway). Due to thermal broadening of the A-exciton resonance at room temperature, the FWM spectra of the gold tip and WSe_2 monolayer are very similar, but the latter FWM response is strongly enhanced due to the large dipole moment of the A-exciton (see Note 7 in the Supporting Information).

We choose a clean monolayer flake of WSe_2, precharacterized by micro-SHG, -2PPL, and -FWM imaging as shown in Figure 2a−c (see Figure S2 for corresponding AFM topography). We then select a representative subregion across the crystal edge (dashed rectangle) which shows no obvious spatial signal variations for corresponding nanoimaging, with the results being shown in Figure 2d−f.

A distinctly higher nanoscale spatial variation is seen in nano-SHG in contrast to both the incoherent 2PPL and coherent FWM images (see Figure S3 for transects and an analysis of spatial resolution). We attribute this higher degree of heterogeneity in SHG to its sensitivity to local symmetry breaking associated with local lattice structural disorder. In contrast, we interpret the lower heterogeneity of FWM as a result of the spatial coherence of the nonlinear polarization across the full evanescent region of $\sim 10^2$−10^4 nm^2 of the tip (see Figure S3 for more details).

For subsequent spatiotemporal FWM nanoimaging, we measure the two-pulse correlation function with time delay (τ) controlled by the pulse shaper. Figure 3a shows the time series of FWM images with increasing time delay of the same sample region as above. The FWM signal decays within a few tens of femtoseconds and with spatial heterogeneity on the 100 nm length scale. Figure 3b shows extracted time traces of the two-pulse correlation function for selected sample regions.

To extract the underlying dephasing time T_2, we describe the induced polarization $\tilde{P}(t) = \int \tilde{R}(t - t')\tilde{E}(t')\,dt'$ based on the response function $\tilde{R}(t)$ with driving field transient $\tilde{E}(t)$. We assume a damped harmonic oscillator behavior $\tilde{R}(t) \propto \exp(i\omega t - t/T_2)$ for the response function. The interferometric two-pulse correlation of the FWM intensity as a function of time delay τ is then given by

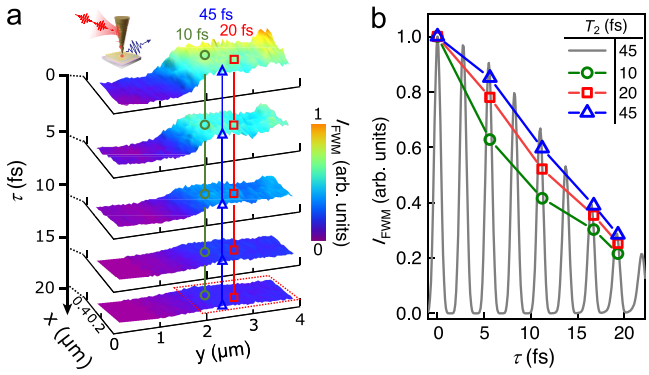

Figure 3. Femtosecond spatiotemporal FWM nanoimaging of monolayer WSe_2. (a) Time series of FWM images for five interpulse delays (from top to bottom) τ = 0, 5.6, 11.2, 16.3, and 19.3 fs. (b) FWM intensities of three selected sample locations for the five delay times with corresponding decoherence times of T_2 = 10, 20, and 45 fs determined by the line envelope. For comparison, a simulated response of T_2 = 45 fs is shown.

$$
\begin{aligned}
I_{FWM}(\tau) \propto \int_{-\infty}^{\infty} dt \iiint_{-\infty}^{\infty} & [(\tilde{P}_1(\omega_1, t) + \tilde{P}_1(\omega_1, t - \tau)] \\
& \times [\tilde{P}_2(\omega_2, t) + \tilde{P}_2(\omega_2, t - \tau)] \\
& \times [\tilde{P}_3(\omega_3, t) + \tilde{P}_3(\omega_3, t - \tau)] \\
& \times \exp[-i(\omega_1 - \omega_2 + \omega_3)t] \\
& \times \delta(\omega - \omega_1 + \omega_2 - \omega_3)\, d\omega_{i=1,2,3}
\end{aligned} \tag{1}
$$

To fit the experimental data, we minimize the residual $r = \sum_i |I_{FWM} - I_i|$ to determine T_2[22] (for details see Note 6 in the Supporting Information). As shown in Figure 3b, for the selected image locations, T_2 values of ∼10, ∼20, and ∼45 fs are obtained with spatial variations on the hundreds of nanometers scale. This behavior is reproducible and representative for different samples, with time scales varying between T_2 < 5 fs and up to ∼60 fs (for additional data see Figure S4).

Following the method above, we extract both T_2 and the corresponding FWM intensity I_{FWM} at τ = 0 fs for each pixel (186 × 186 nm^2) in the sample area indicated by the red dashed rectangle in Figure 3a and plot the result in Figure 4a. Significantly, we observe that regions with the strongest FWM signal correspond to the shortest dephasing times, and vice versa. Figure 4b visualizes this anticorrelation as a contour plot in the T_2 versus I_{FWM} plane. This anticorrelation with weakest FWM emission at locations of longest coherence is unexpected, since one would conventionally expect the intensity of any coherent radiation from an ensemble of excitons to decrease with decreasing T_2.

We first discuss the origin of the FWM response, followed by the decoherence and its spatial heterogeneity, and last, possible mechanisms to explain the observed anticorrelation between FWM intensity and coherence time.

In related FWM measurements of monolayer MoS_2 with an A-exciton energy of ∼1.85 eV using below-exciton-energy femtosecond excitation (∼1.55 eV), the main contribution to the FWM response was assigned to a two-photon resonance between free carrier states (Figure 1c, right pathway).[26−28] In contrast, judging from the FWM spectral behavior, our WSe_2 FWM signal is dominated by the near triply degenerate FWM process (Figure 1c, left pathway). This interpretation is supported by the close spectral proximity of the FWM signal

https://doi.org/10.1021/acs.nanolett.2c04536
Nano Lett. 2023, 23, 1767−1773

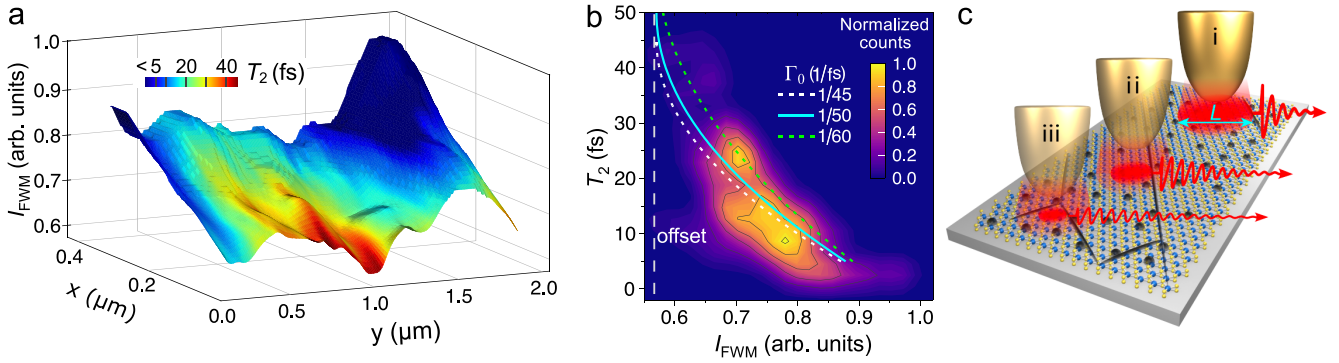

Figure 4. Spatial heterogeneities and T_2−I_{FWM} anticorrelation. (a) Spatial inhomogeneity of T_2 and I_{FWM}, showing anticorrelated behavior. (b) Corresponding plot of T_2 versus I_{FWM}, with the best fit to a model with scattering parameter $\Gamma_0 = 1/50$ fs^{-1} (solid line). (c) Cartoon illustrating the underlying mechanism of spatial coherence of FWM polarization that is nonlocally sensitive to total number of defects within the coherent area, which in turn is controlled by, e.g., grain boundaries, giving rise to a counterintuitive higher I_{FWM} for shorter T_2.

to the strong A-exciton resonance at 1.65 eV (see Figure 1b and Figure S1b, with further details being given in Note 7 in the Supporting Information).

We now compare our room-temperature values of T_2, with spatial variations ranging from $T_2 \lesssim 5$ to $T_2 \gtrsim 60$ fs, with variable-temperature results from other work. Microscale FWM measured on $MoSe_2$ at 6 K showed variations of T_2 from ∼0.5 ps up to 1.5 ps with T_2 being limited by local disorder and associated exciton localization.[10] When the temperature is increased from 6 to 150 K, a decrease of T_2 from 1.4 to 0.2 ps has been interpreted as enhanced exciton−phonon scattering. Theoretical work on the formation, thermalization, and emission of bright (coherent) and dark intra- and intervalley (incoherent) excitons predicted a T_2 value of around 30 fs in WSe_2 at room temperature.[29] For comparison, in the same study on $MoSe_2$, an even shorter value of T_2 of 15 fs was attributed to an efficient formation of incoherent K−K excitons via emission and absorption of acoustic and optical Γ phonons. It should be noted, however, that above-exciton-energy excitation was assumed in these studies, whereas in our case we excite below exciton energy. Room-temperature experimental work investigating valley polaritons in monolayer WSe_2 integrated with a dielectric cavity suggested an underlying exciton dephasing time of ∼60 fs.[30] The range of measurements consistent with these findings assigns the role of defects, substrate interactions, and other spatial heterogeneities to inhomogeneous broadening[10,19−21] and agrees that exciton−phonon and exciton−exciton interactions dominate decoherence.[10,15,16,18] We assign the dramatic shortening of T_2 we observe at room temperature to the strong exciton−phonon scattering accelerating with increasing temperature, in agreement with exciton line width analysis and exciton−phonon scattering theory.[31]

The ultrashort time scales and spatial variation of T_2 observed in our experiments indicate that the dephasing of the nonlinear polarization is dominated by disorder-induced scattering. Even though the third-order response is due to the strong A-exciton resonance at 750 nm, processes involving real exciton populations such as recombination, exciton−exciton, and exciton−phonon scattering likely do not have a significant effect on dephasing in comparison to disorder-induced scattering. This is due to the limited spectral overlap of FWM and pump frequencies with the exciton absorption resonance (see Figure 1b) in below-exciton-energy excitation when compared to situations with resonant or above-gap optical excitation.

One can understand the observed spatial anticorrelation between T_2 and I_{FWM} based on an intuitive picture with minimal model assumptions. In our nanofocusing experiments, an ultrashort broad-band pulse excites a nonlinear polarization in the WSe_2 monolayer across a near-field localized area under the tip. Because the tip radius is much smaller than the FWM wavelengths, the induced localized polarization is spatially coherent over an area L^2, with L being primarily constrained by the tip radius but locally controlled by the distribution of structural features including grain boundaries, line defects, and strain.[32] As the underlying mechanism (Figure 4c), assuming a homogeneous defect density, this would imply a large coherence length in an otherwise unperturbed sample region (i), with associated large FWM dipole moment, yet fast decoherence due to the large number of defects within the large coherence area (L^2). Conversely, if perturbed by, e.g., grain boundaries, the reduced coherence length (ii, iii) then gives rise to a reduced FWM polarization amplitude yet with longer coherence time due to sensing fewer scattering centers. Within L^2, all optical dipoles of excitons oscillate in phase, adding coherently to a net large optical dipole $P(t) \propto L^2$. The resulting FWM polarization of the net time-averaged optical dipole becomes $P_0 \propto L^2 T_2$ and decays with time constant T_2.

In order to phenomenologically model this behavior, we decompose the total decoherence rate $1/T_2 = \Gamma_0 + \Gamma_{dis}$ as the sum of two terms. Here, Γ_0 is the sum of all scattering rates that are unrelated to disorder, such as exciton−phonon scattering. The second term, Γ_{dis}, is disorder-related and varies from location to location. In the absence of specific information about the nature of disorder, we then write the second term for two limiting cases which both lead to the observed anticorrelation effect.

In the first case, the disorder is weak and the scattering of delocalized excitons on the random disorder potential can be treated in the Born approximation. We assume that the disorder-related part of the decoherence rate is due to scattering with uncorrelated point defects with a scattering potential which satisfies $\overline{V(\mathbf{r})V(\mathbf{r}')} = N_{def} V_0^2 \delta(\mathbf{r}' - \mathbf{r})$, where $N_{def} = n_{def} L^2$ is the total number of defects in the coherence area L^2 and V_0 is a constant strength of the disorder potential. Here, n_{def} is the homogeneous defect density of the sample, which we treat as an intrinsic parameter of the sample material. Following the straightforward calculations outlined by Mahan

https://doi.org/10.1021/acs.nanolett.2c04536
Nano Lett. 2023, 23, 1767−1773

et al.[33] and Girvin et al.,[34] the defect scattering rate is then proportional to $N_{def}V_0^2$ and the density of states. With the above approximations, one obtains $\Gamma_{dis} = \alpha L^2$, where the proportionality constant α includes only the intrinsic parameters of the sample which do not vary from spot to spot. The total dephasing rate is then $1/T_2 = \Gamma_0 + \alpha L^2$, where the coherence area L^2 is limited by grain boundaries and varies spatially across the sample. Rearranging to obtain $L^2 \propto -\Gamma_0 + 1/T_2$, we can then eliminate the L^2 term in $P_0 \propto L^2 T_2$ to obtain a model for the FWM intensity as a function of dephasing time given by

$$I_{FWM} \propto P_0^2 \propto (1 - \Gamma_0 T_2)^2 \quad (2)$$

which describes the observed anticorrelation. Note that $\Gamma_0 T_2$ is smaller than 1 by definition.

Since the observed normalized intensity has an overall offset of ~0.6 (Figure 4b), we fit the data with $I_{FWM} \propto 0.6 + 0.4 \times (1 - \Gamma_0 T_2)^2$. We find the best fit using $\Gamma_0 \approx 1/50$ fs^{-1}, which is much longer than the total T_2, again showing that the total dephasing rate is dominated by the disorder-related term $\sim\alpha L^2$.

In the second case, we now consider the opposite limit of strong disorder. Here, excitons are localized on defects and the disorder-related part of the decoherence rate is proportional to the local defect density: $\Gamma_{dis} = \beta n_{def}$. The proportionality constant β does not vary spatially, whereas the defect density n_{def} may vary strongly from point to point. Assuming that the localized excitons make up the main contribution to the FWM signal due to their larger dipole moment compared to free excitons,[35,36] we arrive at the scenario in which the FWM emission from excitons with surface density n_e is proportional to the surface density of defects n_{def}.

In this case, the net dipole formed over the illuminated area would scale as $P \propto n_e \propto n_{def}$, whereas the dephasing rate of the optical dipoles scales with local density of defects as $1/T_2 \sim \Gamma_0 + \beta n_{def}$. Assuming again the radiation intensity to scale as $I_{FWM} \propto P^2 T_2^2 \propto {n_{def}}^2 T_2^2$ and eliminating n_{def}, we obtain the same anticorrelation relation as in eq 2.

Recently, the heterogeneity of T_2 in monolayer $MoSe_2$, MoS_2, and WS_2 was studied on the microscale, observing a similar anticorrelation between homogeneous and inhomogeneous line widths at low temperature, yet in that case it was attributed to the interplay between spatial disorder and radiative lifetime.[19−21] In contrast, in our case we observe an anticorrelation between dephasing time and FWM intensity due to heterogeneous disorder.

In summary, using nonlinear FWM nanoimaging based on few-femtosecond adiabatic nanofocusing as an enabling approach, we resolve the ultrafast electronic decoherence in WSe_2 and its nanoscale heterogeneity at room temperature. We attribute the observed spatial variations of T_2 from $\lesssim 5$ to $T_2 \gtrsim 60$ fs on length scales of 50−100 nm in monolayer WSe_2 on SiO_2 to disorder-induced scattering, with the short time scales resulting from thermally activated exciton−phonon scattering. We discover a novel spatiotemporal anticorrelation between FWM intensity and T_2, with the highest local FWM intensities associated with the shortest dephasing times, or conversely, the longest dephasing times with regions of weakest signal. We describe this behavior, which is contrary to conventional nonlinear optics, as a result of spatial coherence within the subwavelength near-field nonlinear excitation area. This unusual behavior paves the way for using both inherent and artificially structured heterogeneity, such as nanopillar arrays and twisted bilayer 2D materials, to spatially control coherence and nonlinear optical response at the nanoscale. Additionally, this anticorrelation behavior extends the range of novel nonlinear optics phenomena discovered in 2D and other quantum and nanoconfined geometries, including Doppler broadening in graphene,[23] nonlocal nonlinear nanoplasmonics,[24] orientation-dependent exciton−plasmon coupling in heterostructures,[37,38] slow light in WSe_2/plasmonic structures,[39] nanophotocurrent in Weyl semimetals,[40] and tunable SHG in twisted h-BN.[41] Our results thus highlight not only the fundamental challenge associated with heterogeneities in TMDs but also the large playground they provide for a wide range of novel and enhanced optical phenomena in nonlinear nano-optics.

■ ASSOCIATED CONTENT

Supporting Information

The Supporting Information is available free of charge at https://pubs.acs.org/doi/10.1021/acs.nanolett.2c04536.

Micro-Raman, micro-PL spectroscopy, and AFM characterization, line profiles of nano-SHG/2PPL/FWM images, FWM nanoimaging of decoherence from a second sample, dynamics of 2PPL signal, details of the two-pulse correlation model, and description of the FWM identification and pathways (PDF)

■ AUTHOR INFORMATION

Corresponding Authors

Tao Jiang − *MOE Key Laboratory of Advanced Micro-Structured Materials, Shanghai Frontiers Science Center of Digital Optics, Institute of Precision Optical Engineering, and School of Physics Science and Engineering, Tongji University, Shanghai 200092, People's Republic of China;* orcid.org/0000-0001-8656-1738; Email: tjiang@tongji.edu.cn

Alexey Belyanin − *Department of Physics and Astronomy, Texas A&M University, College Station, Texas 77843, United States*; Email: belyanin@physics.tamu.edu

Markus B. Raschke − *Department of Physics and JILA, University of Colorado, Boulder, Colorado 80309, United States;* orcid.org/0000-0003-2822-851X; Email: markus.raschke@colorado.edu

Authors

Wenjin Luo − *MOE Key Laboratory of Advanced Micro-Structured Materials, Shanghai Frontiers Science Center of Digital Optics, Institute of Precision Optical Engineering, and School of Physics Science and Engineering, Tongji University, Shanghai 200092, People's Republic of China; Department of Physics and JILA, University of Colorado, Boulder, Colorado 80309, United States;* orcid.org/0000-0002-4125-9209

Benjamin G. Whetten − *Department of Physics and JILA, University of Colorado, Boulder, Colorado 80309, United States;* orcid.org/0000-0001-5476-3749

Vasily Kravtsov − *School of Physics and Engineering, ITMO University, Saint Petersburg 197101, Russia;* orcid.org/0000-0002-3555-1027

Ashutosh Singh − *Department of Physics and Astronomy, Texas A&M University, College Station, Texas 77843, United States*

Yibo Yang − *Department of Computer Science, University of Colorado, Boulder, Colorado 80309, United States*

https://doi.org/10.1021/acs.nanolett.2c04536
Nano Lett. 2023, 23, 1767−1773

Di Huang − *MOE Key Laboratory of Advanced Micro-Structured Materials, Shanghai Frontiers Science Center of Digital Optics, Institute of Precision Optical Engineering, and School of Physics Science and Engineering, Tongji University, Shanghai 200092, People's Republic of China;* orcid.org/0000-0003-3698-5158

Xinbin Cheng − *MOE Key Laboratory of Advanced Micro-Structured Materials, Shanghai Frontiers Science Center of Digital Optics, Institute of Precision Optical Engineering, and School of Physics Science and Engineering, Tongji University, Shanghai 200092, People's Republic of China;* orcid.org/0000-0002-3855-483X

Complete contact information is available at: https://pubs.acs.org/10.1021/acs.nanolett.2c04536

Author Contributions

W.L., V.K., T.J., and M.B.R. conceived and designed the experiments. W.L. conducted the measurements with support from B.G.W. and guidance from T.J. and M.B.R. A.S. and A.B. provided the theoretical model with help in data interpretation by T.J., D.H., B.G.W., and M.B.R. Y.Y. contributed to the computational data analysis. W.L., D.H., A.B., and M.B.R. wrote the manuscript with the help of all authors.

Notes

The authors declare no competing financial interest.

■ ACKNOWLEDGMENTS

W.L., B.G.W., and M.B.R. acknowledge funding from the US Department of Energy, Office of Basic Sciences, Division of Material Sciences and Engineering, under award no. DESC0008807. A.S. and A.B. acknowledge funding from the Air Force Office for Scientific Research Grant No. FA9550-21-1-0272 and National Science Foundation Award No. 1936276. W.L. and T.J. acknowledge support from the National Natural Science Foundation of China (62005198, 62175188) and the Shanghai Pujiang Program (20PJ1414100). W.L. and X.C. acknowledge support from the National Natural Science Foundation of China (61925504). W.L. acknowledges a fellowship from the International Postdoctoral Exchange Fellowship Program of the Chinese Ministry of Human Resources and Social Security (MoHRSS) (20190052 to W.L.).

■ REFERENCES

(1) Mak, K. F.; Lee, C.; Hone, J.; Shan, J.; Heinz, T. F. Atomically thin MoS_2: a new direct-gap semiconductor. *Phys. Rev. Lett.* **2010**, *105*, 136805.

(2) Liu, X.; Galfsky, T.; Sun, Z.; Xia, F.; Lin, E.-c.; Lee, Y.-H.; Kéna-Cohen, S.; Menon, V. M. Strong light−matter coupling in two-dimensional atomic crystals. *Nat. Photonics* **2015**, *9*, 30−34.

(3) Regan, E. C.; Wang, D.; Paik, E. Y.; Zeng, Y.; Zhang, L.; Zhu, J.; MacDonald, A. H.; Deng, H.; Wang, F. Emerging exciton physics in transition metal dichalcogenide heterobilayers. *Nat. Rev. Mater.* **2022**, *7*, 778−795.

(4) Xia, F.; Wang, H.; Xiao, D.; Dubey, M.; Ramasubramaniam, A. Two-dimensional material nanophotonics. *Nat. Photonics* **2014**, *8*, 899−907.

(5) Mak, K. F.; Shan, J. Photonics and optoelectronics of 2D semiconductor transition metal dichalcogenides. *Nat. Photonics* **2016**, *10*, 216−226.

(6) Xiao, D.; Liu, G.-B.; Feng, W.; Xu, X.; Yao, W. Coupled spin and valley physics in monolayers of MoS_2 and other group-VI dichalcogenides. *Phys. Rev. Lett.* **2012**, *108*, 196802.

(7) Jiang, T.; Liu, H.; Huang, D.; Zhang, S.; Li, Y.; Gong, X.; Shen, Y.-R.; Liu, W.-T.; Wu, S. Valley and band structure engineering of folded MoS_2 bilayers. *Nat. Nanotechnol.* **2014**, *9*, 825−829.

(8) Xu, X.; Yao, W.; Xiao, D.; Heinz, T. F. Spin and pseudospins in layered transition metal dichalcogenides. *Nat. Phys.* **2014**, *10*, 343−350.

(9) Cao, Y.; Fatemi, V.; Fang, S.; Watanabe, K.; Taniguchi, T.; Kaxiras, E.; Jarillo-Herrero, P. Unconventional superconductivity in magic-angle graphene superlattices. *Nature* **2018**, *556*, 43−50.

(10) Jakubczyk, T.; Delmonte, V.; Koperski, M.; Nogajewski, K.; Faugeras, C.; Langbein, W.; Potemski, M.; Kasprzak, J. Radiatively limited dephasing and exciton dynamics in $MoSe_2$ monolayers revealed with four-wave mixing microscopy. *Nano Lett.* **2016**, *16*, 5333−5339.

(11) Xiao, J.; Zhao, M.; Wang, Y.; Zhang, X. Excitons in atomically thin 2D semiconductors and their applications. *Nanophotonics* **2017**, *6*, 1309−1328.

(12) Low, T.; Chaves, A.; Caldwell, J. D.; Kumar, A.; Fang, N. X.; Avouris, P.; Heinz, T. F.; Guinea, F.; Martin-Moreno, L.; Koppens, F. Polaritons in layered two-dimensional materials. *Nat. Mater.* **2017**, *16*, 182−194.

(13) Borri, P.; Langbein, W.; Schneider, S.; Woggon, U.; Sellin, R. L.; Ouyang, D.; Bimberg, D. Ultralong dephasing time in InGaAs quantum dots. *Phys. Rev. Lett.* **2001**, *87*, 157401.

(14) Hao, K.; Moody, G.; Wu, F.; Dass, C. K.; Xu, L.; Chen, C.-H.; Sun, L.; Li, M.-Y.; Li, L.-J.; MacDonald, A. H.; et al. Direct measurement of exciton valley coherence in monolayer WSe_2. *Nat. Phys.* **2016**, *12*, 677−682.

(15) Dey, P.; Paul, J.; Wang, Z.; Stevens, C.; Liu, C.; Romero, A.; Shan, J.; Hilton, D.; Karaiskaj, D. Optical coherence in atomic-monolayer transition-metal dichalcogenides limited by electron-phonon interactions. *Phys. Rev. Lett.* **2016**, *116*, 127402.

(16) Boule, C.; Vaclavkova, D.; Bartos, M.; Nogajewski, K.; Zdražil, L.; Taniguchi, T.; Watanabe, K.; Potemski, M.; Kasprzak, J. Coherent dynamics and mapping of excitons in single-layer $MoSe_2$ and WSe_2 at the homogeneous limit. *Phys. Rev. Mater.* **2020**, *4*, 034001.

(17) Martin, E. W.; Horng, J.; Ruth, H. G.; Paik, E.; Wentzel, M.-H.; Deng, H.; Cundiff, S. T. Encapsulation Narrows and Preserves the Excitonic Homogeneous Linewidth of Exfoliated Monolayer $MoSe_2$. *Phys. Rev. Appl.* **2020**, *14*, 021002.

(18) Moody, G.; Kavir Dass, C.; Hao, K.; Chen, C.-H.; Li, L.-J.; Singh, A.; Tran, K.; Clark, G.; Xu, X.; Berghäuser, G.; et al. Intrinsic homogeneous linewidth and broadening mechanisms of excitons in monolayer transition metal dichalcogenides. *Nat. Commun.* **2015**, *6*, 8315.

(19) Jakubczyk, T.; Nogajewski, K.; Molas, M. R.; Bartos, M.; Langbein, W.; Potemski, M.; Kasprzak, J. Impact of environment on dynamics of exciton complexes in a WS_2 monolayer. *2D Mater.* **2018**, *5*, 031007.

(20) Jakubczyk, T.; Nayak, G.; Scarpelli, L.; Liu, W.-L.; Dubey, S.; Bendiab, N.; Marty, L.; Taniguchi, T.; Watanabe, K.; Masia, F.; et al. Coherence and density dynamics of excitons in a single-layer MoS_2 reaching the homogeneous limit. *ACS Nano* **2019**, *13*, 3500−3511.

(21) Purz, T. L.; Martin, E. W.; Holtzmann, W. G.; Rivera, P.; Alfrey, A.; Bates, K. M.; Deng, H.; Xu, X.; Cundiff, S. T. Imaging dynamic exciton interactions and coupling in transition metal dichalcogenides. *J. Chem. Phys.* **2022**, *156*, 214704.

(22) Kravtsov, V.; Ulbricht, R.; Atkin, J. M.; Raschke, M. B. Plasmonic nanofocused four-wave mixing for femtosecond near-field imaging. *Nat. Nanotechnol.* **2016**, *11*, 459−464.

(23) Jiang, T.; Kravtsov, V.; Tokman, M.; Belyanin, A.; Raschke, M. B. Ultrafast coherent nonlinear nanooptics and nanoimaging of graphene. *Nat. Nanotechnol.* **2019**, *14*, 838−843.

(24) Kravtsov, V.; AlMutairi, S.; Ulbricht, R.; Kutayiah, A. R.; Belyanin, A.; Raschke, M. B. Enhanced third-order optical nonlinearity driven by surface-plasmon field gradients. *Phys. Rev. Lett.* **2018**, *120*, 203903.

(25) Liu, B.; Zhao, W.; Ding, Z.; Verzhbitskiy, I.; Li, L.; Lu, J.; Chen, J.; Eda, G.; Loh, K. P. Engineering bandgaps of monolayer MoS_2 and

WS_2 on fluoropolymer substrates by electrostatically tuned many-body effects. *Adv. Mater.* **2016**, *28*, 6457−6464.
(26) Li, D.; Xiong, W.; Jiang, L.; Xiao, Z.; Rabiee Golgir, H.; Wang, M.; Huang, X.; Zhou, Y.; Lin, Z.; Song, J.; et al. Multimodal nonlinear optical imaging of MoS_2 and MoS_2-based van der Waals heterostructures. *ACS Nano* **2016**, *10*, 3766−3775.
(27) Dai, Y.; Wang, Y.; Das, S.; Li, S.; Xue, H.; Mohsen, A.; Sun, Z. Broadband plasmon-enhanced four-wave mixing in monolayer MoS_2. *Nano Lett.* **2021**, *21*, 6321−6327.
(28) Dai, Y.; Wang, Y.; Das, S.; Xue, H.; Bai, X.; Hulkko, E.; Zhang, G.; Yang, X.; Dai, Q.; Sun, Z. Electrical control of interband resonant nonlinear optics in monolayer MoS_2. *ACS Nano* **2020**, *14*, 8442−8448.
(29) Selig, M.; Berghäuser, G.; Richter, M.; Bratschitsch, R.; Knorr, A.; Malic, E. Dark and bright exciton formation, thermalization, and photoluminescence in monolayer transition metal dichalcogenides. *2D Mater.* **2018**, *5*, 035017.
(30) Qiu, L.; Chakraborty, C.; Dhara, S.; Vamivakas, A. Room-temperature valley coherence in a polaritonic system. *Nat. Commun.* **2019**, *10*, 1513.
(31) Selig, M.; Berghäuser, G.; Raja, A.; Nagler, P.; Schüller, C.; Heinz, T. F.; Korn, T.; Chernikov, A.; Malic, E.; Knorr, A. Excitonic linewidth and coherence lifetime in monolayer transition metal dichalcogenides. *Nat. Commun.* **2016**, *7*, 13279.
(32) Darlington, T. P.; Carmesin, C.; Florian, M.; Yanev, E.; Ajayi, O.; Ardelean, J.; Rhodes, D. A.; Ghiotto, A.; Krayev, A.; Watanabe, K.; et al. Imaging strain-localized excitons in nanoscale bubbles of monolayer WSe_2 at room temperature. *Nat. Nanotechnol.* **2020**, *15*, 854−860.
(33) Mahan, G. D. *Many-particle physics*; Springer: 1990.
(34) Girvin, S. M.; Yang, K. *Modern condensed matter physics*; Cambridge University Press: 2019.
(35) Toropov, A.; Shubina, T.; Jmerik, V.; Ivanov, S.; Ogawa, Y.; Minami, F. Optically enhanced emission of localized excitons in $In_xGa_{1-x}N$ films by coupling to plasmons in a gold nanoparticle. *Phys. Rev. Lett.* **2009**, *103*, 037403.
(36) Wang, H.; Zhang, C.; Chan, W.; Manolatou, C.; Tiwari, S.; Rana, F. Radiative lifetimes of excitons and trions in monolayers of the metal dichalcogenide MoS_2. *Phys. Rev. B* **2016**, *93*, 045407.
(37) Li, Y. J.; Hong, Y.; Peng, Q.; Yao, J.; Zhao, Y. S. Orientation-dependent exciton−plasmon coupling in embedded organic/metal nanowire heterostructures. *ACS Nano* **2017**, *11*, 10106−10112.
(38) Wang, J.; Li, H.; Ma, Y.; Zhao, M.; Liu, W.; Wang, B.; Wu, S.; Liu, X.; Shi, L.; Jiang, T.; et al. Routing valley exciton emission of a WS_2 monolayer via delocalized Bloch modes of in-plane inversion-symmetry-broken photonic crystal slabs. *Light Sci. Appl.* **2020**, *9*, 148.
(39) Klein, M.; Binder, R.; Koehler, M. R.; Mandrus, D. G.; Taniguchi, T.; Watanabe, K.; Schaibley, J. R. Slow light in a 2D semiconductor plasmonic structure. *Nat. Commun.* **2022**, *13*, 6216.
(40) Shao, Y.; Jing, R.; Chae, S. H.; Wang, C.; Sun, Z.; Emmanouilidou, E.; Xu, S.; Halbertal, D.; Li, B.; Rajendran, A.; et al. Nonlinear nanoelectrodynamics of a Weyl metal. *Proc. Natl. Acad. Sci. U.S.A.* **2021**, *118*, e2116366118.
(41) Yao, K.; Finney, N. R.; Zhang, J.; Moore, S. L.; Xian, L.; Tancogne-Dejean, N.; Liu, F.; Ardelean, J.; Xu, X.; Halbertal, D.; et al. Enhanced tunable second harmonic generation from twistable interfaces and vertical superlattices in boron nitride homostructures. *Sci. Adv.* **2021**, *7*, eabe8691.

https://doi.org/10.1021/acs.nanolett.2c04536
Nano Lett. 2023, 23, 1767−1773